



CHORUS

This is the accepted manuscript made available via CHORUS. The article has been published as:

Dislocation core structures in Ni-based superalloys
computed using a density functional theory based flexible
boundary condition approach

Anne Marie Z. Tan, Christopher Woodward, and Dallas R. Trinkle

Phys. Rev. Materials **3**, 033609 — Published 28 March 2019

DOI: [10.1103/PhysRevMaterials.3.033609](https://doi.org/10.1103/PhysRevMaterials.3.033609)

Dislocation core structures in Ni-based superalloys computed using density functional theory-based flexible boundary condition approach

Anne Marie Z. Tan,^{1,2} Christopher Woodward,^{3,*} and Dallas R. Trinkle^{1,†}

¹*Department of Materials Science and Engineering,
University of Illinois at Urbana-Champaign, Urbana, IL 61801, USA*

²*Department of Materials Science and Engineering,
University of Florida, Gainesville, FL 32611, USA*

³*Materials and Manufacturing Directorate, Air Force Research Laboratory,
Wright Patterson Air Force Base, Dayton, OH 45433-7817, USA*

(Dated: February 15, 2019)

Abstract

Nickel-based superalloys are widely used in applications requiring high strength, creep and fatigue resistance at elevated temperatures. Such structural properties are controlled by the glide and cross-slip of screw dislocations in the Ni matrix and Ni₃Al precipitates. The strengthening mechanisms are determined in turn by screw dislocation core structures that are difficult to image with WB-TEM. Core structures of two primary superalloy deformation modes, $1/2\langle 110 \rangle$ Ni screw and $\langle 110 \rangle$ Ni₃Al screw super dislocation, are predicted using density functional theory with flexible boundary conditions.

Keywords: dislocations; intermetallics; density-functional theory

I. INTRODUCTION

Nickel-based superalloys' high strength, creep and fatigue resistance are derived from their microstructure which consist of a face-centered cubic (FCC) Ni matrix containing 40% to 80% volume fraction of L_{12} Ni_3Al precipitates¹. The structural properties of both these phases are strongly influenced by the core structure of the active dislocation deformation modes. The cross-slip of ordinary $\frac{1}{2}\langle 110 \rangle$ and $\langle 110 \rangle$ super dislocations in Ni and Ni_3Al respectively affect work hardening and high temperature strength. $\frac{1}{2}\langle 110 \rangle$ -type dislocations in FCC Ni spontaneously dissociate into Shockley partials bounding an intrinsic stacking fault (ISF) to lower the total energy (c.f. Fig. 1):

$$\frac{1}{2}[1\bar{1}0] \rightarrow \frac{1}{6}[2\bar{1}\bar{1}] + \text{ISF} + \frac{1}{6}[1\bar{2}1]. \quad (1)$$

The L_{12} crystal structure is an ordered FCC derivative lattice in which the minority and majority species occupy the cube corners and face centers, respectively, doubling the periodicity of the crystal along the $\langle 110 \rangle$ direction. Ni_3Al produces $\langle 110 \rangle$ -type superdislocations which dissociate into two $\frac{1}{2}\langle 110 \rangle$ -type superpartials bounding an antiphase boundary (APB); while the superpartials dissociate into Shockley partials bounding complex stacking faults (CSF):

$$\begin{aligned} [1\bar{1}0] &\rightarrow \frac{1}{2}[1\bar{1}0] + \text{APB} + \frac{1}{2}[1\bar{1}0] \\ &\rightarrow \left(\frac{1}{6}[2\bar{1}\bar{1}] + \text{CSF} + \frac{1}{6}[1\bar{2}1] \right) + \text{APB} + \left(\frac{1}{6}[2\bar{1}\bar{1}] + \text{CSF} + \frac{1}{6}[1\bar{2}1] \right) \end{aligned} \quad (2)$$

An APB produces chemical disorder at the boundary, while a CSF combines the structural disorder of an ISF with the chemical disorder of an APB (c.f. Figs. 1 and 2). Cross-slip of these superpartials leads to an increase in strength with increasing temperature (anomalous yield strength²⁻⁴), which is a key factor in the success of superalloys. The probability of cross-slip is controlled by the distance between the Shockley partials⁵. Accurate determination of the equilibrium core structures of Ni and Ni_3Al screw dislocations is crucial to modeling anomalous yield stress and creep mechanisms in Ni-based superalloys.

Given the importance of dislocations in superalloys, both experimental and modeling efforts have provided qualitative and quantitative information about dislocation geometry. Experimental estimates for dislocation core structures in Ni and Ni_3Al have all been based on measurements of the splitting distance of the Shockley partials for edge or mixed dislocations⁶⁻⁹. This is because the edge dislocations spread significantly wider than the screw dislocations and can therefore be more accurately resolved in weak beam transmission electron microscopy (TEM) experiments. For

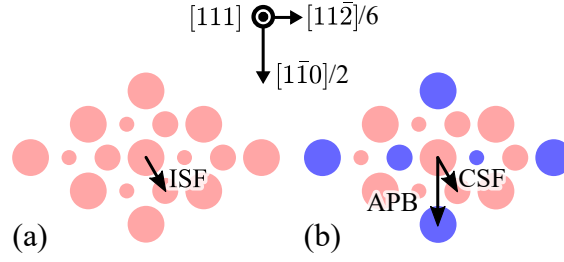


FIG. 1. The slip vectors that create (a) an intrinsic stacking fault (ISF) in FCC Ni, and (b) an antiphase boundary (APB) and a complex stacking fault (CSF) in $L1_2$ Ni_3Al . Pink atoms represent Ni atoms and blue atoms represent Al atoms. The different atom sizes indicate atoms on different close-packed (111) planes.

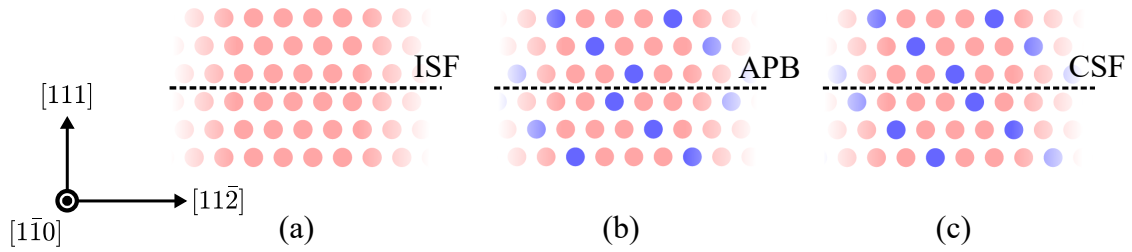


FIG. 2. Side views of (a) an intrinsic stacking fault (ISF) in FCC Ni, (b) an antiphase boundary (APB), and (c) a complex stacking fault (CSF) in $L1_2$ Ni_3Al . Pink atoms represent Ni atoms and blue atoms represent Al atoms. The ISF creates structural disorder across the fault plane, the APB creates only chemical disorder, and the CSF creates both structural and chemical disorder.

Ni, with a Poisson ratio of ≈ 0.276 , anisotropic elasticity theory predicts the ratio of equilibrium splitting distances is $d_{\text{edge}}/d_{\text{screw}} = 7/3^{10}$. The distance between the edge Shockley partials is then used to estimate the stacking fault (complex stacking fault) energy using anisotropic elasticity theory (AET). In turn the separation of the Shockley partials in the screw dislocations are estimated using this energy and AET. This creates a problem when one is trying to model the properties of a dislocation core using the experimentally measured planar fault energies. For example, the important feature for dislocation cross-slip is the distance between the Shockley partials, and what stress is required to form the constricted (screw) dislocation. The stacking fault energy is only relevant if the anisotropic elastic solution precisely maps the splitting distance.

Atomistic simulations suggest that there is a systematic error between the actual core splitting distances and those predicted by AET, but this has never been explored or verified using density

functional theory (DFT). The screw dislocation in Ni has been relaxed using various empirical potentials which predict a wide range of stacking fault energies and dissociation distances^{11–13}. The planar fault energies in Ni^{14,15} and Ni₃Al^{16–18} have been computed from first principles, with Schoeck *et al.*¹⁶ and Mryasov *et al.*¹⁷ using these energies as inputs to a Peierls-Nabarro model to compute dissociation distances in Ni₃Al, while Yu *et al.*¹⁸ used the planar fault energies and isotropic elasticity theory to estimate these distances. While these computational studies have provided insights into active deformation mechanisms, they are at best approximations of the core structures, with limited utility in predicting the effects of variations in chemistry and kinetics. Here, we assess if the differences observed between atomistic and AET predictions for the Shockley core splitting distances are replicated in first principles calculations of dislocation cores in Ni and Ni₃Al.

Modeling the electronic structure of an isolated dislocation is challenging due to the long-range strain field. This requires a multiscale approach that couples the core — where there are large strains — to the long range elastic field. While anisotropic continuum elasticity theory^{19,20} describes the far-field geometry around a dislocation well, the elastic solution diverges close to the core and electronic structure methods (i.e. DFT) are needed to accurately determine the dislocation core structure. Moreover, the long-range strain field of an isolated dislocation is incompatible with periodic or fixed boundary conditions which are commonly used in DFT simulations. Multiscale approaches which couple the dislocation core to finite elements^{21,22}, classical potentials^{23,24}, or flexible boundary conditions (FBC)²⁵ have been developed to accurately capture both the core structure as well as the long-range strain field of the dislocation by coupling the quantum mechanical core to a continuum. This work focuses on the FBC method²⁵, in which atoms near the dislocation core are relaxed by DFT while atoms outside the core are displaced according to the lattice Green function (LGF), effectively embedding the dislocation within an infinite harmonic bulk. Calculation of the LGF goes back to simple cubic lattices with nearest-neighbor interactions^{26,27} to arbitrary Bravais lattices²⁸ to arbitrary crystals²⁹ and even a planar interface³⁰. Recently, we developed a new numerical method to compute the LGF which directly accounts for the dislocation topology³¹. Here, we extend our numerical method developed in Ref.³¹ to compute the LGF for more complex crystal structures including an extended fault geometry, and compute the relaxed dislocation core structures of the $\frac{1}{2}[1\bar{1}0]$ Ni screw dislocation and the $[1\bar{1}0]$ Ni₃Al superdislocation with DFT.

II. COMPUTATIONAL METHODOLOGY

A. DFT setup details

The dislocation cores in Ni and Ni₃Al are calculated using density functional theory as implemented in the Vienna *ab initio* simulation package `vASP`³² which is based on plane wave basis sets. The calculations used the Perdew-Burke-Ernzerhof generalized gradient approximation exchange-correlation functional³³ and projector-augmented wave potentials³⁴ generated by Kresse and Joubert³⁵ with electronic configurations of [Ar]3d⁸4s² and [Ne]3s²3p¹ to model Ni and Al. For fcc Ni, spin-polarized calculations were performed employing a plane wave cutoff energy of 400 eV which ensures energy convergence to within 1 meV/atom. In order to facilitate rapid convergence of the Brillion zone integration, Methfessel-Paxton smearing³⁶ with smearing energy width of 0.25 eV was used with a $1 \times 1 \times 12$ Monkhorst-Pack k -point mesh³⁷. The calculations for Ni₃Al used the spin-averaged approximation, a plane wave cutoff energy of 337 eV, Methfessel-Paxton smearing (0.10 eV) and a $1 \times 1 \times 11$ k -point mesh.

We compute the lattice and elastic constants and planar fault energies in Ni and Ni₃Al using DFT, which we use to estimate dissociation distances from anisotropic elasticity theory for comparison with the values obtained from our relaxations. The computed lattice and elastic constants for Ni: $a_0 = 3.5219$ Å, $C_{11} = 270.4$ GPa, $C_{12} = 157.1$ GPa, $C_{44} = 129.4$ GPa, and for Ni₃Al: $a_0 = 3.5685$ Å, $C_{11} = 226.4$ GPa, $C_{12} = 153.7$ GPa, $C_{44} = 118.9$ GPa, have been previously computed and reported in¹. We compute the planar fault energies by taking the difference in total energy per fault area between two supercells with and without the fault. For the stacking fault in Ni, we construct the faulted supercell by shortening the periodic distance along the direction perpendicular to the fault plane from $8 \cdot [111]$ to $(8-1/3) \cdot [111]$, essentially removing a close-packed plane and thus changing the stacking order at the fault. We compute the Ni stacking fault energy γ_{ISF} using a $10 \times 1 \times 12$ k -point mesh. For the planar faults in Ni₃Al, we apply alias shear³⁸ to construct a single APB or CSF in $1 \times 3 \times 1$ supercells. The shear vectors required to construct an APB and a CSF are $[1\bar{1}0]/2$ and $[11\bar{2}]/6$, respectively. We compute γ_{APB} and γ_{CSF} using these sheared supercells and $4 \times 1 \times 6$ k -point meshes. The computed lattice and elastic constants and planar fault energies are used as inputs to the equations presented in Appendix A to obtain anisotropic elasticity estimates of the dissociation distances for each dislocation.

Figure 3 shows the DFT supercells used to relax a $\frac{1}{2}[1\bar{1}0]$ screw dislocation in Ni and a $[1\bar{1}0]$

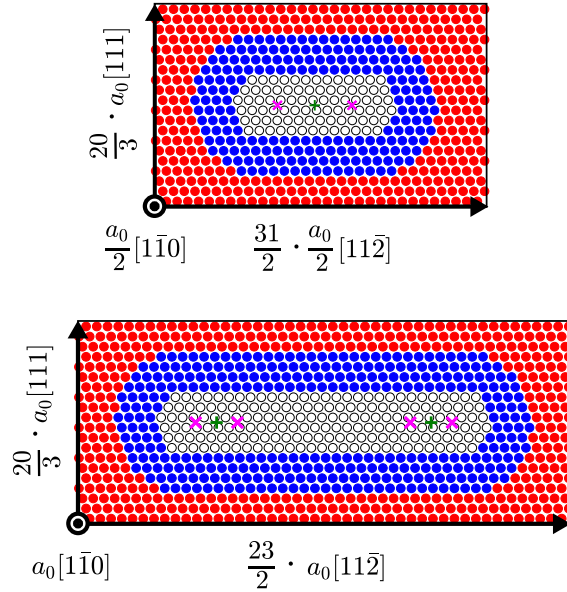


FIG. 3. DFT supercells for the (top) FCC Ni $\frac{1}{2}[1\bar{1}0]$ screw dislocation and (bottom) L1₂ Ni₃Al $[1\bar{1}0]$ screw superdislocation. The atoms in each supercell are divided into three regions for applying flexible boundary conditions. For Ni₃Al, each atom pictured in the figure represents a column of two non-equivalent atoms along the $[1\bar{1}0]$ direction within the supercell. Green plus signs (+) show the initial positions of $\frac{1}{2}[1\bar{1}0]$ screw dislocation(s), and magenta crosses (×) indicate estimated Shockley partial distances from previous studies^{11,17}.

screw superdislocation in Ni₃Al respectively. Supercells are constructed with fractional supercell vectors rather than the typical integer multiples of lattice vectors in order to partially cancel the stacking faults formed at the supercell boundaries due to the screw dislocation and to minimize the disruption to the charge density at the boundaries³⁹. The atoms in each supercell are divided into three racetrack-shaped regions (Figure 3). The interior (Region 1) contains atoms closest to the partial dislocations and planar fault(s). A single $\frac{1}{2}[1\bar{1}0]$ screw dislocation is introduced in the center of Region 1 (Figure 3a) using displacements from anisotropic elasticity theory. To speed up convergence of the Ni₃Al superdislocation, two $\frac{1}{2}[1\bar{1}0]$ screw superpartials $\approx 44 \text{ \AA}$ apart¹⁷ were introduced into Region 1 (Figure 3b). The atoms in region 1 are then relaxed using DFT Hellmann-Feynman forces and conjugate gradients. This allows the (super) partials to dissociate, following the reactions described in Eqns. 1 and 2. The Hellmann-Feynman forces that develop in the annular region (region 2) are relatively small (i.e. linear) and are passed through the LGF to displace the atoms throughout the simulation cell¹¹. Region 3 contains atoms in the supercell

necessary to minimize the effect of the supercell boundaries on the atoms in regions 1 and 2. Using DFT forces on atoms in regions 1 and 2, we alternate between relaxing region 1 with conjugate gradients and displacing atoms in all three regions due to LGF displacements from forces in region 2, until forces in regions 1 and 2 are smaller than 5 meV/Å.

B. Lattice Green function computation

The LGF is computed by inversion of a large, sparse matrix of force constants that correspond to the atomic positions in the dislocation geometry³¹. The force-constants — which relate the force on an atom to the displacement of any atom in the system — are short-ranged and bulk-like even as one approaches the core. For simple crystal structures such as FCC Ni, we have shown that the force constants between a pair of atoms in the dislocation geometry can be well approximated by the closest equivalent pair of atoms in the bulk³¹.

However, the APB in the $[1\bar{1}0]$ Ni₃Al superdislocation creates pairs of atoms of different atomic species than are found in bulk, and the corresponding force constants are not defined. For example, there are only Ni–Ni and Ni–Al first-nearest-neighbors in bulk, but the APB creates Al–Al first-nearest-neighbors as well (c.f. Figure 2). Since we use the force-constants from bulk to approximate the force-constants in the dislocation geometry, we do not have force-constants for such pairs of atoms, which we refer to as “antisite” pairs. Instead, we approximate these force-constants by performing a constrained linear least squares fit which enforces the symmetry of the overall force constant matrix by enforcing symmetry of the onsite terms:

$$D_{\alpha\beta}(\vec{R}_i, \vec{R}_i) = D_{\beta\alpha}(\vec{R}_i, \vec{R}_i), \quad (3)$$

which gives 3 constraint equations for each atom i with at least one “antisite” neighbor. By the sum rule, we can rewrite this as

$$-\sum_{j \neq i} D_{\alpha\beta}(\vec{R}_i, \vec{R}_j) = -\sum_{j \neq i} D_{\beta\alpha}(\vec{R}_i, \vec{R}_j), \quad (4)$$

where atoms $j \neq i$ are all the neighbors of atom i . Separating the contributions to this sum from “antisite” neighbors j_A and “bulk-like” neighbors j_B and rearranging the terms, we get

$$\sum_{j_A} D_{\alpha\beta}(\vec{R}_i, \vec{R}_{j_A}) - \sum_{j_A} D_{\beta\alpha}(\vec{R}_i, \vec{R}_{j_A}) = -\sum_{j_B} D_{\alpha\beta}(\vec{R}_i, \vec{R}_{j_B}) + \sum_{j_B} D_{\beta\alpha}(\vec{R}_i, \vec{R}_{j_B}), \quad (5)$$

where the unknown force-constants are all on the left hand side of the equation. The number of unknowns is $9 \times (\text{number of “antisite” pairs})$ which is typically much larger than the number

of constraints. Therefore, we perform a linear least squares fit to the average of the known bulk Ni₃Al force-constants for each type of neighbor pair (e.g. first-nearest-neighbors, second-nearest-neighbors, etc.) to find the most physical solution from among all the possible solutions that satisfy the constraints. While this is a rather rough estimate, we find that as long as these force constants are contained entirely in region 1, they have only a weak effect on the LGF for atoms in regions 2 and 3³¹.

The dislocation force-constant matrix is numerically inverted following the method developed previously³¹. The method requires setting up a large system divided into five regions: regions 1–3 which make up the DFT supercell, a buffer region, and a far-field. The far-field contains atoms far away from the core whose displacements we approximate using the bulk elastic Green function (EGF), while the buffer region contains the remaining atoms between region 3 and the far-field. Strictly speaking, this assumption is valid only for perfect bulk crystals; when a dislocation is present, the long-range behavior of the dislocation LGF is not necessarily given by the bulk EGF^{40,41}. However, we have found this to be a reasonably good approximation if the distance from the center of the dislocation to the far-field atoms is large compared to the dislocation core dimensions. For the Ni $\frac{1}{2}[1\bar{1}0]$ screw dislocation we choose a buffer size of $R = 20a_0$ (≈ 70 Å), while for the Ni₃Al $[1\bar{1}0]$ screw superdislocation—since the initial dislocation geometry has an extended size of ≈ 44 Å—we choose a larger system size of $R = 40a_0$ (≈ 143 Å) for computing the LGF. We verify that the errors in the LGF computation due to the far-field approximation are on the order of $10^{-4}\text{Å}^2/\text{eV}$ or less. We compute the LGF for forces in region 2 by applying a unit force on an atom in region 2, evaluating the resulting far-field displacements based on the EGF, determining the forces these displacements generate in the buffer region, then solving for the displacements corresponding to the initial force by numerically inverting the force-constant matrix. This gives us one column of the LGF; by systematically looping through every atom in region 2, we can compute the required portion of the LGF matrix that gives displacements in regions 1–3 due to forces in region 2.

III. RESULTS

Figure 4 shows that the $\frac{1}{2}[1\bar{1}0]$ screw dislocation in Ni dissociates into two Shockley partials. Differential displacement (DD) maps⁴² and Nye tensor distributions⁴³ are overlaid⁴⁴ for the screw components (top figure) and edge components (bottom figure) of the relaxed screw dislocation.

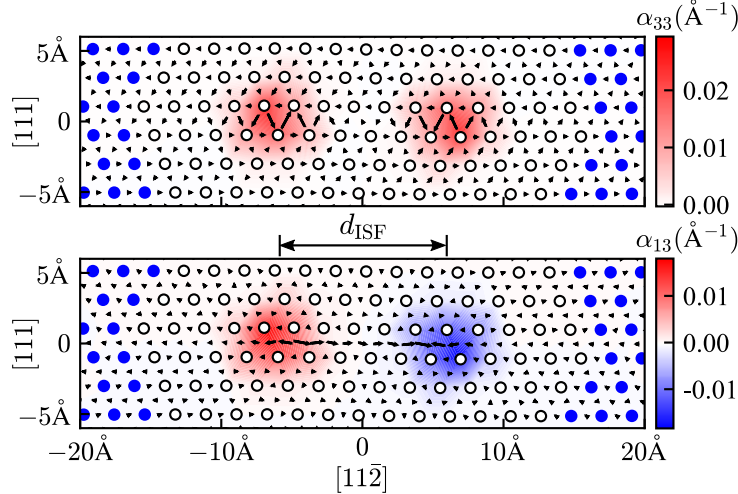


FIG. 4. Combined differential displacement and Nye tensor distribution plots for the (top) screw and (bottom) edge components of the relaxed FCC Ni $\frac{1}{2}[1\bar{1}0]$ screw dislocation. These plots show all the atoms in region 1 (white atoms) and a few atoms from region 2 (blue atoms). The edge displacements in the bottom plot are scaled by a factor of 10 to be visible compared with the screw components in the top plot. We estimate $d_{\text{ISF}} = 12.0 \text{ \AA}$.

The partial cores are well separated from Region 2, indicating good convergence. Estimated $d_{\text{ISF}} = 12.0 \text{ \AA}$ is 40% larger than the 8.6 \AA separation estimated from anisotropic elasticity theory using DFT-computed elastic constants and intrinsic stacking fault energy¹ (see Appendix A).

Table I compares the Ni intrinsic stacking fault energy γ_{ISF} and dissociation distance d_{ISF} to other computational studies and experiments, where we see a consistent difference between d_{ISF} direct from atomistic simulations versus the elastic estimate. Our computed γ_{ISF} of 123.6 mJ/m^2 is in good agreement with other DFT-computed values reported in literature^{14,15}. This is the first work to report the first principles assessment of the Ni screw dislocation core structure, although there have been a number of studies which relaxed the dislocation using empirical potentials^{11–13}. While empirical potentials predict a wide range of γ_{ISF} and d_{ISF} , they all produce d_{ISF} from atomistic relaxation that is 28–73% larger than the corresponding elastic estimate. The wide range of empirical potential predictions highlights the need for accurate first-principles calculations. Our computed γ_{ISF} is in good agreement with values extracted from experiment; however, there are no direct observations of the dissociated screw dislocation in Ni with which to compare our results. Murr⁴⁵ estimated γ_{ISF} based on its relationship to the coherent twin-boundary energy, while Carter *et al.* estimated it based on observations of dissociated edge dislocations and faulted dipoles. It

TABLE I. Comparison of calculated and experimental intrinsic stacking fault energies γ_{ISF} and dissociation distances d_{ISF} for the $\frac{1}{2}[1\bar{1}0]$ screw dislocation in Ni. This work (PAW-GGA + LGF) is the first to predict a Ni screw dislocation core using DFT. We find a partial separation larger than the anisotropic elasticity theory estimate, which is consistent with empirical potential calculations. Experimental studies extracted γ_{ISF} based on the coherent twin-boundary energy (Murr⁴⁵) or observations of dissociated edge dislocations and faulted dipoles (Carter *et al.*⁶); we compute the corresponding experimental elastic estimates for d_{ISF} using Eq. (A1) and elastic constants from Simmons and Wang⁴⁶.

	γ_{ISF} (mJ/m ²)	$d_{\text{ISF}}(\text{\AA})$	
		Atomistic	P-N Elastic
DFT:			
PAW-GGA + LGF	123.6	12.0	8.6
PAW-GGA ¹⁴	127.2		
PAW-GGA ¹⁵	136.2		
Empirical potential:			
EAM + LGF ¹¹	58	19.5	15.2
EAM + LGF ¹¹	119	13.0	7.5
EAM ¹²	176		7.4
Finnis-Sinclair ¹³	40	25.0	15.25
Experiment:			
Bright field TEM ⁴⁵	128		7.1
Weak beam TEM ⁶	120–130		7.0–7.6

should also be noted that the stacking fault energy has some temperature dependence⁴⁷, where it is estimated to decrease by less than 10% from 0K to 300K. We compute the corresponding experimental elastic estimates for d_{ISF} listed in the table using Eq. (A1) and elastic constants from Simmons and Wang⁴⁶.

Figure 5 shows that the $[1\bar{1}0]$ superdislocation in Ni₃Al dissociates into two pairs of Shockley partials, where the APB and CSF are formed between the partials as expected by Eqn. 2. Similar to Fig. 4, the DD maps and Nye tensor distributions are overlaid for the screw components (top figure) and edge components (bottom figure) of the relaxed screw superdislocation⁴⁴. Again, all the Shockley partials have the same screw components and alternating edge components with an

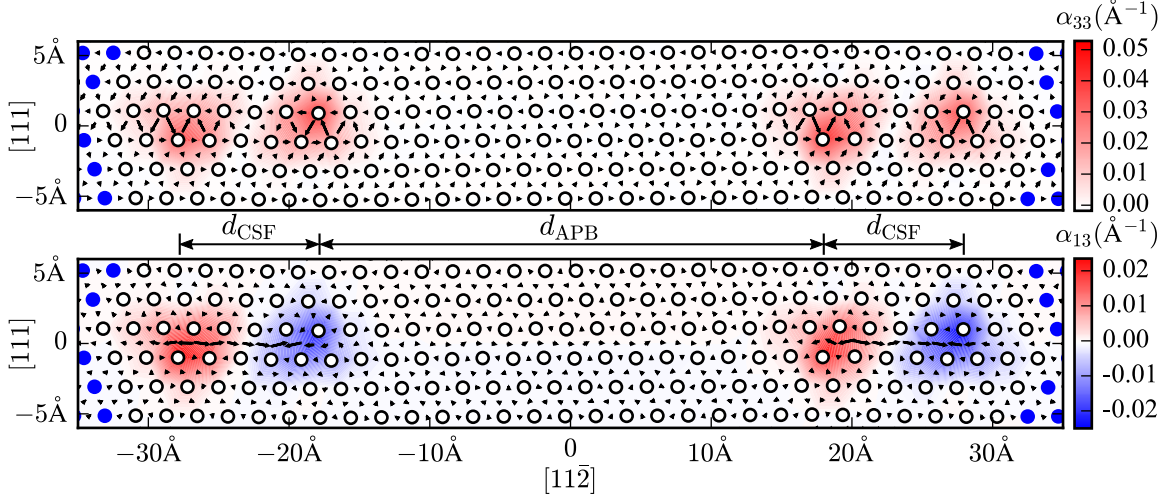


FIG. 5. Combined differential displacement and Nye tensor distribution plots for the (top) screw and (bottom) edge components of the relaxed $L1_2$ Ni_3Al $[1\bar{1}0]$ screw superdislocation. As there are two layers of atoms within the slab, we compute the differential displacements and Nye tensor as averages through the slab thickness. These plots show all the atoms in region 1 (white atoms) and a few atoms from region 2 (blue atoms). The edge displacements in the bottom plot are scaled by a factor of 10 to be visible compared with the screw components in the top plot. We estimate $d_{\text{APB}} = 36.4 \text{ \AA}$ and $d_{\text{CSF}} = 10.0 \text{ \AA}$.

estimated partial core splitting: $d_{\text{APB}} = 36.4 \text{ \AA}$ and $d_{\text{CSF}} = 10.0 \text{ \AA}$, while $d_{\text{APB}} = 32.8 \text{ \AA}$ and $d_{\text{CSF}} = 6.4 \text{ \AA}$ from anisotropic elasticity theory and DFT-computed elastic constants¹ (see Appendix A). Anisotropic elasticity underestimates both d_{APB} and d_{CSF} by 3.6 \AA , similar to the discrepancy between the computed and estimated values of d_{ISF} for the Ni screw dislocation.

Table II compares the dissociation distances d_{APB} and d_{CSF} computed in this work—the first first-principles assessment of the Ni_3Al screw superdislocation core structure—to other computational studies and experiments. Due to the complex extended dislocation structure, such calculations are extremely challenging and computationally expensive. FBC supercell requires 1840 atoms; without FBC, even larger supercells would be required to accurately compute the dislocation structure, making the problem intractable. Our dissociation distances are in generally good agreement with those computed by previous studies using Peierls-Nabarro model^{16,17} or elasticity theory¹⁸. However, the key advantage of our approach compared to these continuum models is we have the atomic-level details of the core geometry that can be used to predict how different chemical species will interact with these dislocation cores. These atomic scale interactions have been shown to be critical in understanding the effects of chemistry on plastic deformation^{52,53}. We

TABLE II. Comparison of calculated and experimental planar fault energies γ_{APB} and γ_{CSF} and dissociation distances d_{APB} and d_{CSF} for the $[1\bar{1}0]$ screw superdislocation in Ni_3Al . This work (PAW-GGA + LGF) produces separations larger than estimated from anisotropic elasticity theory. While Schoeck *et al.*¹⁶, Mryasov *et al.*¹⁷ and Yu *et al.*¹⁸ computed the planar fault energies with DFT, Schoeck *et al.* and Mryasov *et al.* computed d_{APB} and d_{CSF} using a Peierls-Nabarro model, while Yu *et al.* simply estimated these distances from isotropic elasticity theory. We also compute d_{APB} and d_{CSF} using the Mishin EAM potential⁴⁸. The experimental studies (Hemker *et al.*⁷, Karnthaler *et al.*⁸, Kruml *et al.*⁹) estimated γ_{APB} and γ_{CSF} based on observations of dissociated edge or mixed dislocations; we compute the corresponding screw dislocation dissociation distances d_{APB} and d_{CSF} using Eqs. (A4) and (A5) and elastic constants from Prikhodko *et al.*⁴⁹.

	γ_{APB}	γ_{CSF}	$d_{\text{APB}}(\text{\AA})$			$d_{\text{CSF}}(\text{\AA})$		
	(mJ/m ²)	(mJ/m ²)	Atomistic	P-N	Elastic	Atomistic	P-N	Elastic
DFT:								
PAW-GGA + LGF	171.2	202.4	36.4		32.8	10.0		6.4
LAPW-LDA ¹⁶	172	223		33			6.25	
LMTO-LDA ¹⁷	210	225		34.3±8	36.0		8.7±1	5.3
PAW-GGA ¹⁸	178.76	202.32			36.01			8.76
Empirical potential:								
EAM	252	202	19		19.9	12		10.0
EAM ⁵⁰	142	121	60 - d_{CSF}		41.7	60 - d_{APB}		18.3
EAM ⁵¹	156	259	60 - d_{CSF}			60 - d_{APB}		
Experiment:								
Weak beam TEM ⁷	180±20	206±30			32.1			6.8
Weak beam TEM ⁸	175±15	235±40			34.5			5.4
Weak beam TEM ⁹	195±13	236±29			30.2			5.8

note that the planar configuration studied in this work is only one possible configuration that the extended superdislocation can take. We have focused on this configuration because early computational studies based on elastic models and classical potentials predicted that the planar configuration is the most energetically stable compared to non-planar and mixed configurations^{50,51,54}. Other configurations may be of interest for consideration in future work, and could also be treated

with the method described in this work, given slightly different initial conditions.

IV. DISCUSSION

In both cases explored in this work the Shockley partial splitting distance was observed to be larger than that expected from anisotropic elasticity theory. Also, as shown in Tables I and II, atomistic calculations reproduce this effect across a wide range of potentials. The results presented here suggest that the conventional application of anisotropic elasticity theory produces a systematic error that should be considered when developing models for cross-slip.

Analysis of our relaxed dislocation geometries reveal that the maximum edge displacement achieved in each of the Shockley partials is in fact only about 2/3 of the expected edge component. The edge components in the Shockley partials can be calculated from the atomic positions in the relaxed dislocation cores. In the Ni $\frac{1}{2}[1\bar{1}0]$ screw dislocation, the expected edge component is $\frac{\sqrt{6}}{12}a_0 = 0.719\text{\AA}$, but the maximum edge displacement is only 0.487\AA or 67.7% of the expected edge component. Similarly, in the Ni₃Al $[1\bar{1}0]$ screw superdislocation, the expected edge component is $\frac{\sqrt{6}}{12}a_0 = 0.728\text{\AA}$, but the maximum edge displacement is only 0.467\AA or 64.1% of the expected edge component. The expressions derived from AET which are used to estimate the splitting distances assume ideal splitting in which the partials achieve the full edge components; however, our results indicate that this assumption is not valid and is the likely reason for the systematic discrepancy between AET estimates and results from atomistic simulations. Reevaluating the elastic estimates using Eqs. (A1), (A4) and (A5) and the reduced edge components, we find $d_{\text{ISF}}^{\text{el}} = 13.2\text{\AA}$ and $d_{\text{CSF}}^{\text{el}} = 10.3\text{\AA}$ which are in better agreement with our DFT-computed dissociation distances.

The error in estimated dissociation distances introduced by employing AET based on the idealized dissociated dislocations could lead to significant errors when modeling cross-slip mechanisms in Ni-superalloys. In Ni we can estimate the scale of the error introduced by employing the anisotropic elastic mapping between our DFT-computed stacking fault energy ($\gamma_{\text{ISF}}^{\text{DFT}}$) and Shockley splitting distances obtained from relaxation with GGA-LGF ($d_{\text{ISF}}^{\text{DFT}}$). We can derive an effective Escaig stress, showing the effect of using the classical anisotropic theory,

$$\gamma_{\text{ISF}}^{\text{DFT}} d_{\text{ISF}}^{\text{DFT}} = (\gamma_{\text{ISF}}^{\text{DFT}} + \sigma_{\text{E}} b_e) d_{\text{ISF}}^{\text{el}} \quad (6)$$

On the left are the DFT-computed values, on the right an Escaig stress σ_{E} acting on the edge components b_e of the screw Shockley partials is added to the DFT-computed stacking fault energy,

and multiplied by the splitting distance derived using AET. Using $\gamma_{\text{ISF}}^{\text{DFT}} = 123.6 \text{ mJ/mm}^2$, $d_{\text{ISF}}^{\text{DFT}} = 12\text{\AA}$, $d_{\text{ISF}}^{\text{el}} = 8.6\text{\AA}$ gives an effective Escaig stress of 670 MPa. Following Kang, Yin and Cai⁵⁵, applying this Escaig stress changes the activation energy for cross-slip in Ni from 2.25 to 1.25 eV. Thus the stress (or temperature) required to enable cross-slip is decreased by approximately 50% using the first principles observations. A similar argument holds for the anomalous yield stress; the corresponding equations for estimating the Escaig stress in Ni₃Al are:

$$(\gamma_{\text{CSF}}^{\text{DFT}} - \gamma_{\text{APB}}^{\text{DFT}}/2)d_{\text{CSF}}^{\text{DFT}} = (\gamma_{\text{CSF}}^{\text{DFT}} - \gamma_{\text{APB}}^{\text{DFT}}/2 + \sigma_{\text{E}}b_e)d_{\text{CSF}}^{\text{el}} \quad (7)$$

Using the values from Table II, the effective Escaig stress introduced using the anisotropic model of Shockley partial spreading is $\approx 900 \text{ MPa}$. Thus the effects are large on the scale of the stresses required to close the Shockley partial splitting distances to permit cross-slip.

It is important for the materials community to have reliable representation of the screw dislocations in engineering alloys in order to accurately model cross-slip. Cross-slip can influence work hardening through multiplication processes and in ordered intermetallics, such as Ni₃Al, cross-slip can produce anomalous yield stress at elevated temperatures. Recently Kang, Yin and Cai have shown using atomistic potentials that the energy barrier for cross-slip in Ni is strongly dependent on (Escaig) stresses that act on the edge components of the Shockley partials and affect the partial core splitting distance⁵⁵. Similarly, the anomalous yield stress behavior observed in Ni₃Al is controlled by the cross-slip of super dislocations from (111) to (100) glide planes. In this case the Shockley partials that are required to constrict to form a screw (super) partial bracket a complex stacking fault. Our results imply that by using anisotropic elasticity theory to map the splitting distance to a planar fault energy introduces an effective Escaig stress which will bias analytical models of cross-slip. Therefore a more accurate method of determining the core structures and dissociation distances of these dislocations—such as has been presented in this work—is crucial in order to accurately model cross-slip mechanisms in Ni-based superalloys.

V. CONCLUSION

Core structures of screw dislocations in Ni and Ni₃Al are predicted using a DFT-based flexible boundary condition approach. Differences between predicted dissociation distances and those estimated from Peierls-Nabarro models or elasticity theory demonstrate the limitations of these continuum models and highlights the need for accurate atomistic calculations. The calculated

atomic-level details of the core geometry are required for further studies of solid solution or diffusion near or along a dislocation. The computed dissociation distances can also be used to parameterize higher length scale models to study the anomalous yield stress and creep mechanisms in Ni-based superalloys. The current extension of the FBC approach enables calculations for a wide variety of extended dislocation cores and can be applied to dislocations in a range of technologically important materials including metals, ordered intermetallics, and semiconductors.

ACKNOWLEDGMENTS

This research was supported by NSF/DMR Grant No. 1410596 and a grant of computer time from the DOD High Performance Computing Modernization Program, at the Air Force Research Laboratory Major Shared Resource Center.

Appendix A: Estimating dissociation distances from elasticity theory

We compute the dissociation distances for each dislocation from anisotropic elasticity theory in order to compare against the values obtained from our relaxations. We compute the intrinsic stacking fault distance d_{ISF} in the $\frac{1}{2}[1\bar{1}0]$ Ni screw dislocation from anisotropic elasticity theory by balancing the elastic interaction between the partial dislocations against the stacking fault energy γ_{ISF} . This yields the following expression for d_{ISF} :

$$d_{\text{ISF}} = \frac{K_s b_{1s} b_{2s} + K_e b_{1e} b_{2e}}{2\pi\gamma_{\text{ISF}}} \quad (\text{A1})$$

where b_{is} and b_{ie} are the magnitudes of the screw and edge components of the Burgers vector \vec{b}_i of partial dislocation i (for this dislocation, $b_{1s} = b_{2s} = \frac{1}{2}\frac{\sqrt{2}}{2}a_0$ and $b_{1e} = -b_{2e} = \frac{1}{\sqrt{12}}\frac{\sqrt{2}}{2}a_0$) and K_s and K_e are the screw and edge components of the elastic energy coefficients derived in¹⁰,

$$K_s = (c'_{44}c'_{55})^{1/2} \quad (\text{A2})$$

$$K_e = \frac{(\bar{c}'_{11} + c'_{12})}{3} \left[2 \left(\frac{c'_{55}(\bar{c}'_{11} - c'_{12})}{c'_{22}(\bar{c}'_{11} + c'_{12} + 2c'_{55})} \right)^{1/2} + \left(\frac{c'_{55}(\bar{c}'_{11} - c'_{12})}{c'_{11}(\bar{c}'_{11} + c'_{12} + 2c'_{55})} \right)^{1/2} \right] \quad (\text{A3})$$

where the c'_{ij} are the elastic constants rotated into the $[001]$, $\frac{1}{\sqrt{2}}[\bar{1}\bar{1}0]$, $\frac{1}{\sqrt{2}}[1\bar{1}0]$ coordinate system, and $\bar{c}'_{11} = (c'_{11}c'_{22})^{1/2}$. Following a similar approach, we compute the antiphase boundary distance

d_{APB} and complex stacking fault distance d_{CSF} in Ni_3Al from anisotropic elasticity theory by balancing the elastic interactions between the partial dislocations against the relevant planar fault energies. The force balance equations for the two leftmost partials with Burgers vectors \vec{b}_1 and \vec{b}_2 are:

$$\frac{K_s b_{1s} b_{2s} + K_e b_{1e} b_{2e}}{2\pi d_{\text{CSF}}} + \frac{K_s b_{1s} b_{3s} + K_e b_{1e} b_{3e}}{2\pi(d_{\text{CSF}} + d_{\text{APB}})} + \frac{K_s b_{1s} b_{4s} + K_e b_{1e} b_{4e}}{2\pi(2d_{\text{CSF}} + d_{\text{APB}})} = \gamma_{\text{CSF}} \quad (\text{A4})$$

$$-\frac{K_s b_{2s} b_{1s} + K_e b_{2e} b_{1e}}{2\pi d_{\text{CSF}}} + \frac{K_s b_{2s} b_{3s} + K_e b_{2e} b_{3e}}{2\pi d_{\text{APB}}} + \frac{K_s b_{2s} b_{4s} + K_e b_{2e} b_{4e}}{2\pi(d_{\text{CSF}} + d_{\text{APB}})} = -\gamma_{\text{CSF}} + \gamma_{\text{APB}} \quad (\text{A5})$$

where γ_{APB} and γ_{CSF} are the antiphase boundary energy and complex stacking fault energy respectively, $b_{1s} = b_{2s} = b_{3s} = b_{4s} = \frac{1}{2} \frac{\sqrt{2}}{2} a_0$, $b_{1e} = -b_{2e} = b_{3e} = -b_{4e} = \frac{1}{\sqrt{12}} \frac{\sqrt{2}}{2} a_0$, and the expressions for the elastic energy coefficients K_s and K_e are as defined previously in Eq. (A2) and Eq. (A3). By symmetry, the forces on the other pair of Shockley partials are equal and opposite. We solve this pair of non-linear equations numerically to obtain the elastic estimates for d_{APB} and d_{CSF} .

* christopher.woodward@us.af.mil

† dtrinkle@illinois.edu

¹ C. Woodward, A. van de Walle, M. Asta, and D. R. Trinkle, *Acta Mater.* **75**, 60 (2014).

² V. Paidar, D. Pope, and V. Vitek, *Acta Metall.* **32**, 435 (1984).

³ D. Pope, “Physical metallurgy,” (Elsevier, Amsterdam, 1996) Chap. Mechanical Properties of Intermetallic Compounds, pp. 2075–2104, 4th ed.

⁴ P. Veyssi re and G. Saada, “Dislocations in solids,” (Elsevier, Amsterdam, 1996) Chap. Microscopy and plasticity of the $\text{L1}_2 \gamma'$ phase, pp. 253–441.

⁵ A. Paxton and Y. Sun, *Phil. Mag. A* **78**, 85 (1998).

⁶ C. B. Carter and S. M. Holmes, *Phil. Mag.* **35**, 1161 (1977).

⁷ K. J. Hemker and M. J. Mills, *Phil. Mag. A* **68**, 305 (1993).

⁸ H. P. Karnthaler, E. T. M hlbacherand, and C. Rentenberger, *Acta Mater.* **44**, 547 (1996).

⁹ T. Kruml, E. Conforto, B. L. Piccolo, D. Caillard, and J. L. Martin, *Acta Mater.* **50**, 5091 (2002).

¹⁰ J. P. Hirth and J. Lothe, *Theory of Dislocations*, 2nd ed. (Wiley, New York, 1982).

¹¹ S. Rao, T. A. Parthasarathy, and C. Woodward, *Phil. Mag. A* **79**, 1167 (1999).

¹² P. Szelestey, M. Patriarca, and K. Kaski, *Modell. Simul. Mater. Sci. Eng.* **11**, 883 (2003).

- 13 Y. Qi, A. Strachan, T. Cagin, and W. A. Goddard, III, *Mater. Sci. Eng., A* **309–310**, 156 (2001).
- 14 M. Chandran and S. K. Sondhi, *J. Appl. Phys.* **109**, 103525 (2011).
- 15 F. Bianchini, J. Kermode, and A. D. Vita, *Modell. Simul. Mater. Sci. Eng.* **24**, 045012 (2016).
- 16 G. Schoeck, S. Kohlhammer, and M. Fahnle, *Phil. Mag. Lett.* **79**, 849 (1999).
- 17 O. N. Mryasov, Y. N. Gornostyrev, M. van Schilfgaarde, and A. J. Freeman, *Acta Mater.* **50**, 4545 (2002).
- 18 X.-X. Yu and C.-Y. Wang, *Phil. Mag.* **92**, 4028 (2012).
- 19 A. Stroh, *J. Math. Phys.* **41**, 77 (1962).
- 20 D. J. Bacon, D. M. Barnett, and R. O. Scattergood, *Prog. Mater. Sci.* **23**, 51 (1980).
- 21 E. B. Tadmor, M. Ortiz, and R. Phillips, *Philos. Mag. A* **73**, 1529 (1996).
- 22 G. Lu, E. B. Tadmor, and E. Kaxiras, *Phys. Rev. B* **73**, 024108 (2006).
- 23 N. Choly, G. Lu, W. E, and E. Kaxiras, *Phys. Rev. B* **71**, 094101 (2005).
- 24 Z. C. Y. Liu, G. Lu and N. Kioussis, *Model. Simul. Mater. Sci. Eng* **15**, 275 (2007).
- 25 J. E. Sinclair, P. C. Gehlen, R. G. Hoagland, and J. P. Hirth, *J. Appl. Phys.* **49**, 3890 (1978).
- 26 V. K. Tewary, *Adv. Phys.* **22**, 757 (1973).
- 27 I. R. MacGillivray and C. A. Sholl, *J. Phys. F* **13**, 23 (1983).
- 28 D. R. Trinkle, *Phys. Rev. B* **78**, 014110 (2008).
- 29 J. A. Yasi and D. R. Trinkle, *Phys. Rev. E* **85**, 066706 (2012).
- 30 M. Ghazisaeidi and D. R. Trinkle, *Phys. Rev. B* **82**, 064115 (2010).
- 31 A. M. Z. Tan and D. R. Trinkle, *Phys. Rev. E* **94**, 023308 (2016).
- 32 G. Kresse and J. Furthmüller, *Phys. Rev. B* **54**, 11169 (1996).
- 33 J. P. Perdew, K. Burke, and M. Ernzerhof, *Phys. Rev. Lett.* **77**, 3865 (1996).
- 34 P. E. Blöchl, *Phys. Rev. B* **50**, 17953 (1994).
- 35 G. Kresse and D. Joubert, *Phys. Rev. B* **59**, 1758 (1999).
- 36 M. Methfessel and A. T. Paxton, *Phys. Rev. B* **40**, 3616 (1989).
- 37 H. J. Monkhorst and J. D. Pack, *Phys. Rev. B* **13**, 5188 (1976).
- 38 M. Jahnátek, J. Hafner, and M. Krajčí, *Phys. Rev. B* **79**, 224103 (2009).
- 39 C. Woodward, *Mater. Sci. Eng., A* **400-401**, 59 (2005).
- 40 V. K. Tewary, *Phys. Rev. B* **69**, 094109 (2004).
- 41 V. Tewary, in *Modeling, Characterization, and Production of Nanomaterials*, Woodhead Publishing Series in Electronic and Optical Materials, edited by V. K. Tewary and Y. Zhang (Woodhead Publishing,

2015) pp. 55 – 85.

- ⁴² V. Vitek, R. C. Perrin, and D. K. Bowen, *Phil. Mag.* **21**, 1049 (1970).
- ⁴³ C. S. Hartley and Y. Mishin, *Acta Mater.* **53**, 1313 (2005).
- ⁴⁴ C. Woodward, D. R. Trinkle, L. G. Hector, and D. L. Olmsted, *Phys. Rev. Lett.* **100**, 045507 (2008).
- ⁴⁵ L. E. Murr, *Scripta Met.* **6**, 203 (1972).
- ⁴⁶ G. Simmons and H. Wang, *Single Crystal Elastic Constants and Calculated Aggregate Properties: A Handbook*, 2nd ed. (MIT Press, Cambridge, MA, 1971).
- ⁴⁷ S. L. Shang, W. Y. Wang, Y. Wang, Y. Du, J. X. Zhang, A. D. Patel, and Z. K. Liu, *J. Phys.: Cond. Matt.* **24**, 155402 (2012).
- ⁴⁸ Y. Mishin, *Acta Mater.* **52**, 1451 (2004).
- ⁴⁹ S. V. Prikhodko, H. Yang, A. J. Ardell, J. D. Carnes, and D. G. Isaak, *Metall. Mater. Trans. A* **30**, 2403 (1999).
- ⁵⁰ R. Pasionot, D. Farkas, and E. J. Savino, *Scripta Metall. Mater.* **24**, 1669 (1990).
- ⁵¹ M. H. Yoo, M. S. Daw, and M. J. Baskes.
- ⁵² D. R. Trinkle and C. Woodward, *Science* **310**, 1665 (2005).
- ⁵³ G. P. M. Leyson, W. A. Curtin, L. G. Hector Jr, and C. F. Woodward, *Nat. Mater.* **9**, 750 (2010).
- ⁵⁴ M. Yamaguchi, V. Paidar, D. P. Pope, and V. Vitek, *Phil. Mag. A* **45**, 867 (1982).
- ⁵⁵ K. Kang, J. Yin, and W. Cai, *J. Mech. Phys. Solids* **62**, 181 (2014).